JMEPEG (2007) 16:254–264
DOI: 10.1007/s11665-007-9046-y

1059-9495/$19.00

A Comparison of Aging Kinetics of New and Rejuvenated Conventionally Cast GTD-111 Gas Turbine Blades

E. Lvova

(Submitted July 31, 2006)

Two industrial gas turbine blades made from a conventionally cast Ni-base superalloy GTD-111, one new and the other rejuvenated, were removed from the same machine after a particular operational cycle for an examination in order to determine the effect of rejuvenation on the material's behavior during service. It was found that service-induced changes in the microstructure, such as γ′-phase coarsening and coalescence, excessive grain-boundary secondary $M_{23}C_6$ carbides formation, and primary MC carbides decomposition, were noticeably more advanced in the rejuvenated blade. The stress-rupture life of the rejuvenated blade decreased significantly compared to that of the new blade after the same number of hours in service. The cause of this decrease appears to be related to a release of additional amounts of carbon and carbide-forming elements into the matrix during rejuvenating heat treatment as a result of the primary MC carbide decomposition.

Keywords aging kinetics, gas turbine blades, rejuvenation, superalloys

1. Introduction

Hot section blades of a modern industrial gas turbine are expected to withstand high temperatures and stresses during long-time service, which can cause both surface and internal damage thus reducing mechanical properties and reliability of the blades. Extensive studies have shown that a prolonged thermal and stress exposure causes "overaging" of the microstructure (γ′-phase coarsening and coalescence, formation of continuous secondary $M_{23}C_6$ carbide films on the grain boundaries, primary MC carbide degeneration, TCP phase formation), which has detrimental effects on the component's properties and, consequently, service life (Ref 1-6).

The cost of replacement of the modern blades is very high. A lot of effort is being put to extend the service life of the components. Advanced coating systems are applied to protect hot section blade surface. Rejuvenating processes and heat treatments have been developed that allow serviced blades to be refurbished and returned to service for an additional operational cycle.

The implementation of the rejuvenating procedures, such as solution-and-aging heat treatment and Hot Isostatic Pressing (HIP) has proven to be able to restore even severely overaged blade microstructure and properties to a virtually "as-new" condition (Ref 1, 4, 7-11). They are currently employed successfully throughout the industry. However, there is not much data on the behavior of rejuvenated blades in the next service cycle. It was the objective of this investigation to study the influence of rejuvenation on the processes taking place in the blade during the subsequent operational cycle.

E. Lvova, GE Preco – Metallurgical Laboratory, 17619 Aldine Westfield Rd, Houston, TX 77073. Contact e-mail: evgenia.lvova@ge.com.

2. Experimental Procedure

Two 1st-stage blades removed from the same GE MS7001E industrial gas turbine, after completing an operational cycle, were provided for this study courtesy of the company-owner of this turbine. The turbine worked in a base-load mode, with a firing temperature 1120 °C. The blades will be further referenced to as Blade 1 and Blade 2.

Blade 1 had been put into the machine as new and served for 12,781 h. Blade 2 had been refurbished by the third party vendor after 24,000 h of original service, then it had been returned to service in the same set as the Blade 1 to run for additional 12,781 h.

It should be noted that having a new blade and a rejuvenated blade serve in one set is an uncommon occurrence. Normally, the set consists of the blades of one service history. This unique opportunity of having one new and one rejuvenated blade from the same machine after the service cycle in the same set was used to study the influence of rejuvenation on the material's behavior during service.

Both blades are made from a conventionally cast (CC) Ni-base superalloy GTD-111. The chemical compositions of the blades are given in Table 1.

Based on the information obtained from the company-turbine owner, Blade 1 had the external MCrAlY coating and internal aluminide coating on the cooling holes. Blade 2 had originally similar external and internal coatings, which were stripped prior to rejuvenation.

According to the turbine owner, Blade 2 had undergone a rejuvenating heat treatment (HIP had not been performed). Blade 2 had been re-coated with the external and internal coatings identical to those of Blade 1. The standard coating

Table 1 Chemical compositions of the examined blades

Elements	Elemental concentration, wt.%	
	Blade 1	Blade 2
Carbon	0.09	0.09
Chromium	13.84	13.98
Cobalt	9.28	9.31
Aluminum	3.05	3.03
Titanium	4.93	4.93
Molybdenum	1.57	1.59
Tungsten	3.75	3.73
Tantalum	2.94	2.94
Iron	0.05	0.05
Vanadium	0.04	0.04
Hafnium	0.02	0.02
Zirconium	0.005	0.006
Boron	0.013	0.014
Silicon	0.03	0.02
Nickel	Balance	Balance

diffusion heat treatments were incorporated into rejuvenating heat treatment. The details of rejuvenating and coating diffusion heat treatments were considered a proprietary information of the vendor.

The specimens for a metallographic examination were cut from the shank and from the airfoil leading and trailing edges at approximately ½ airfoil height; the specimens for stress-rupture tests were cut from the shank and from the middle of the airfoil (Fig. 1). All specimens were sectioned by the wire EDM process. The metallographic specimens were etched electrolytically with 2% water solution of chromic trioxide (Cr_2O_3) or chemically with Kalling's reagent (5 g $CuCl_2$ + 3 mL HNO_3 + 50 mL ethanol).

The examination of the microstructure was performed using an optical microscope and a scanning electron microscope (SEM). Backscattered electron imaging (BEI) was used to examine the as-polished surfaces. The quantitative analysis of phase volume fraction based on the contrast produced by backscattered electrons was used. Energy-dispersive x-ray spectroscopy (EDS) system with thin window light element detector was used to determine the elemental concentration of various phases. The elemental distribution x-ray maps were generated.

Thin foil specimens were prepared using standard methods and examined in a transmission electron microscope (TEM) equipped with EDS system. Convergent beam electron diffraction and standard selected area electron diffraction methods were used.

The microhardness of the metallographic specimens was measured as per ASTM E384; load, 500 g, magnification, 550×.

Stress-rupture tests were performed as per ESTM139. The cylinder specimens had the gauge length of 20 mm with the diameter 4 mm. The test conditions: temperature 815 °C, constant load 480 MPa. The test conditions were chosen with the purpose to achieve a compromise between simulating the service conditions and allowing the tests to be completed within a reasonable time (time to fracture approximately 100 h for a new material). Although relatively short term compared to more accurate 2000 h tests, the 100 h tests proved to be reliable enough to correlate with the information obtained by other methods employed in combination.

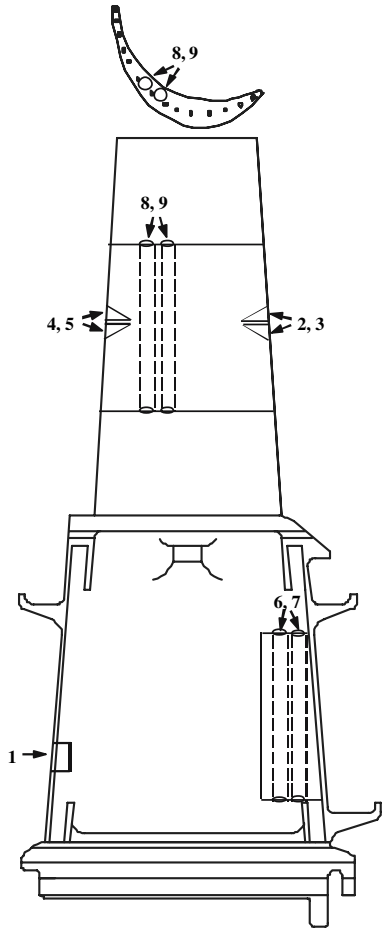

Fig. 1 The blade section plan. 1—shank section 25 mm×20 mm; 2, 3—leading edge sections 25 mm long; 4, 5—trailing edge sections 25 mm long; 6, 7—cylinder bars from the shank for the stress-rupture tests specimens; 8, 9—cylinder bars from the airfoil for the stress-rupture tests specimens

3. Results and Discussion

3.1 Shank Specimens

The shank metal served as an indicator of the initial metal condition, since the service temperature of the shank was relatively low and did not cause a degradation of the microstructure during service. The maximum service-induced damage of the blade material from a combination of high temperature and operating stresses occurred in the middle of the airfoil. The comparison of the microstructures of the shank and the middle-airfoil specimens (leading edge and trailing edge) was used to determine the changes generated by the service.

The microstructures of the Blade 1 and Blade 2 shank specimens were identical and typical of a new CC GTD-111 superalloy (Fig. 2).

The microstructure constituents were: austenitic fcc γ-matrix; ordered fcc Ni_3(Al, Ti) γ′-phase precipitated coherently with the matrix; massive irregularly shaped primary MC carbides, with well-defined edges, formed at the grain boundaries and in the grain interiors during solidification; and fine globular secondary $M_{23}C_6$ carbides decorating the grain boundaries. The γ′-phase demonstrated bimodal morphology:

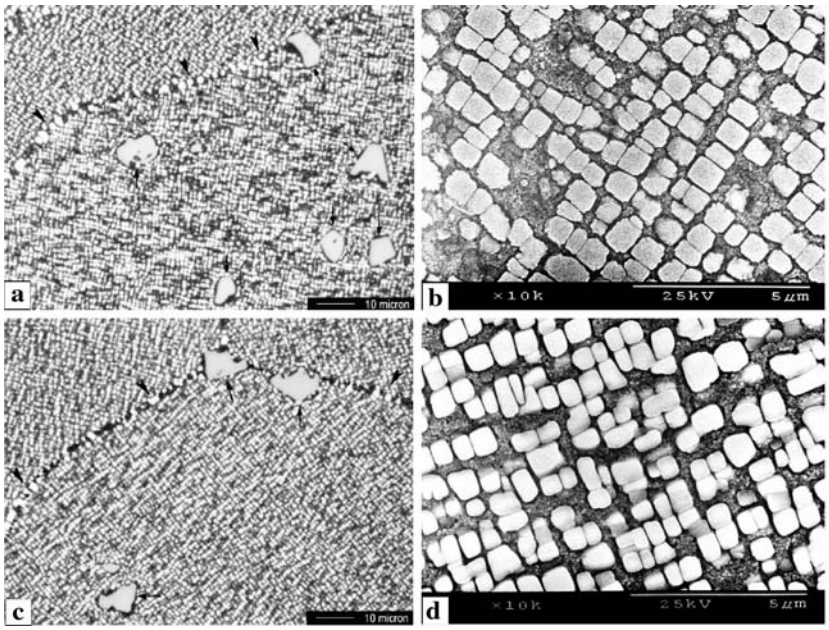

Fig. 2 Optical micrographs of the shank specimens of Blade 1 (a) and Blade 2 (c); SEM micrographs of the shank specimens of Blade 1 (b) and Blade 2 (d). Arrows indicate primary MC carbides at the grain boundaries and in the grain interiors; arrowheads indicate secondary $M_{23}C_6$ carbides at the grain boundaries (Etchant—electrolytic chromic acid)

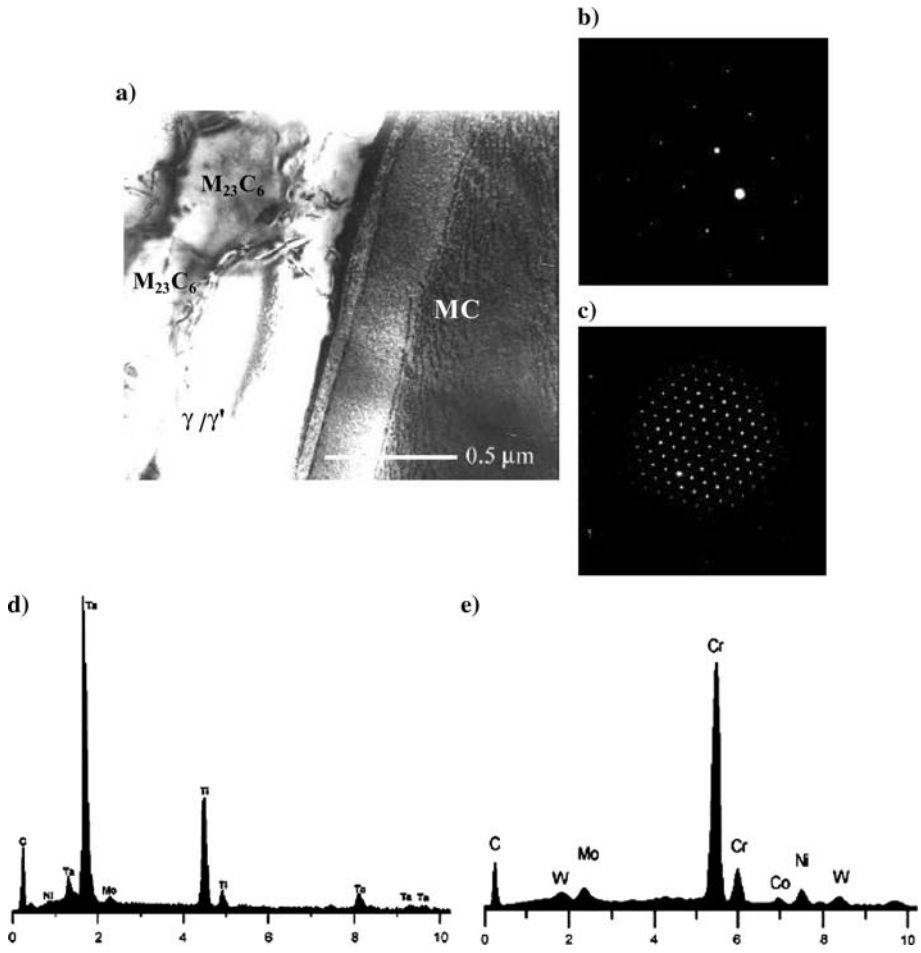

Fig. 3 Bright-field TEM micrograph of the Blade 1 shank (a); selected-area diffraction patterns (SADP) from MC (b) and $M_{23}C_6$ (c); EDS spectra from MC (d) and $M_{23}C_6$ (e)

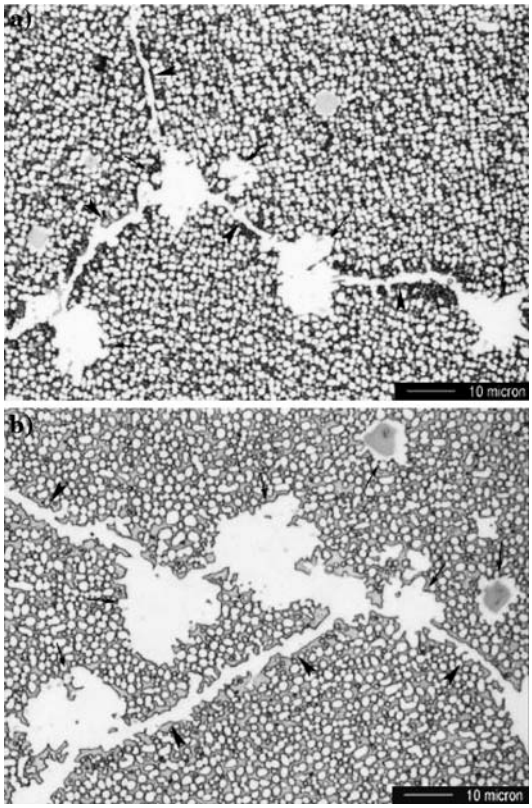

Fig. 4 Optical micrographs of the Blade 1 (a) and Blade 2 (b) leading edge specimens. Arrows indicate degenerated primary MC carbides; arrowheads indicate excessive secondary $M_{23}C_6$ carbide precipitation at the grain boundaries (Etchant—electrolytic chromic acid)

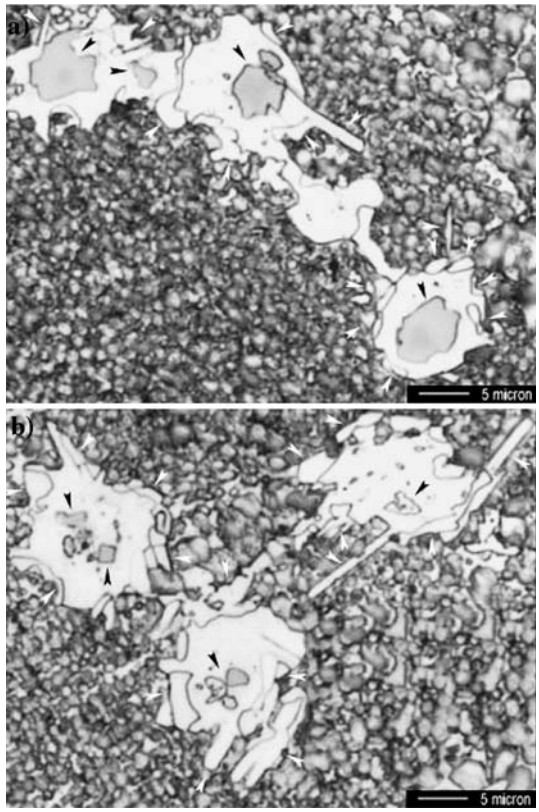

Fig. 5 Optical micrographs of the degenerated primary MC carbides in leading edge specimens of Blade 1 (a) and Blade 2 (b). Black arrowheads indicate remnants of the original MC carbides surrounded by decomposition zone. White arrowheads indicate M23C6 carbides formed at the periphery of decomposition zone as discrete particles and as laths (Etchant—Kalling's reagent)

primary cuboidal γ' with an average side size 0.69 μm in the Blade 1 and 0.62 μm in the Blade 2, and secondary spheroidal γ'.

The bright-field TEM micrograph in Fig. 3(a) showed the MC carbide situated at the grain boundary, which was decorated with small $M_{23}C_6$ carbides. Selected-area diffraction patterns from MC and $M_{23}C_6$ carbides (Fig. 3b, c, respectively) revealed no orientation relationship between them indicating their independent nucleation. $M_{23}C_6$ carbides obeyed cube-cube orientation relationship with the fcc γ matrix: $\{100\}_{M_{23}C_6} || \{100\}_{\gamma}$, $\langle 100\rangle_{M_{23}C_6} || \langle 100\rangle_{\gamma}$.

The EDS spectra demonstrated that primary MC carbides were rich in tantalum and titanium: (Ta, Ti)C (Fig. 3d), and $M_{23}C_6$ carbides were rich in chromium: $Cr_{23}C_6$ (Fig. 3e).

3.2 Airfoil Specimens

The microstructures of the leading edge and trailing edge specimens were examined in the areas close to the surfaces and in the center of the 25 mm long sections. There was no appreciable difference in the microstructure appearance throughout the sections.

The external and internal coatings in both blades remained intact, the base metal was protected from environmental attack.

The optical micrographs of the Blade 1 and Blade 2 leading edge specimens presented in Fig. 4 displayed significant service-induced microstructural changes compared to the respective shank specimens. The microstructures of the trailing edge specimens were similar to those of the leading edges.

The airfoil microstructures of both new Blade 1 and rejuvenated Blade 2 demonstrated features typically found in the hot section blades retired from service: excessive secondary $M_{23}C_6$ carbide precipitation at the grain boundaries, γ' particles coarsening and agglomeration, and primary MC carbides decomposition.

Numerous studies had shown that the service-induced microstructural changes affected the blade material properties (Ref 1-6). The presence of dense grain-boundary secondary carbide precipitates forming a continuous network can assist crack propagation that leads to a reduction of creep-resistance properties. Coarsening and coalescence of γ' particles lessens the precipitation-hardening effect. Primary MC carbide decomposition promotes secondary carbide formation. The growing secondary carbides consume chromium from the matrix, consequently diminishing the solution-strengthening effect and the heat resistance of the alloy.

It is known that the decomposition of primary MC carbides in Ni-base superalloys is accompanied by the formation of $M_{23}C_6$ carbides. It is believed that $M_{23}C_6$ carbides and γ'-phase form in the area surrounding the disintegrated MC carbide. In accordance with the currently accepted viewpoint, the primary MC carbide decomposition follows the reaction (Ref 3, 6, 12):

$$MC + \gamma \rightarrow M_{23}C_6 + \gamma'. \quad \text{(Eq 1)}$$

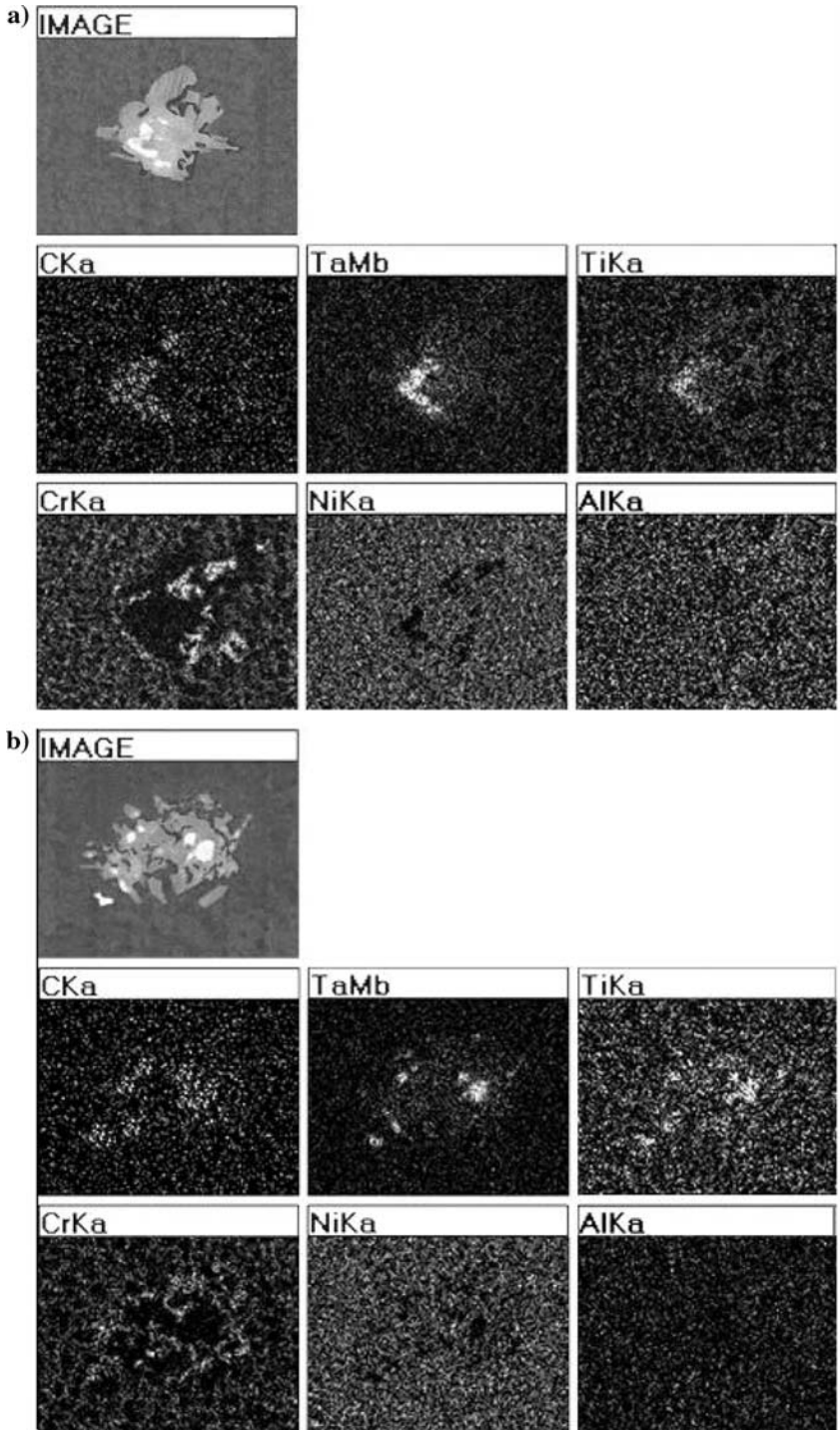

Fig. 6 X-ray maps of the primary MC carbides in the Blade 1 (a) and Blade 2 (b) leading edge specimens

In both blades MC carbide decomposition resulted in a considerable reduction of its size or in breaking down in to several pieces (Fig. 5). The disintegrated MC carbides were surrounded by a well-defined decomposition zone, with discrete $M_{23}C_6$ carbides precipitating at its periphery. The $M_{23}C_6$ carbides formed in the lath-like morphology as well, originating on the MC/γ interface.

The x-ray maps showed the elemental distribution in the degenerated MC carbides (Fig. 6). It can be seen that in both blades remnants of the decomposed MC carbide were rich in Ta and Ti, as the original carbides. High concentration of chromium can be noted on the MC periphery; this fact is consistent with the $M_{23}C_6$ carbide formation as a result of MC carbide decomposition. No evidence of increased concentrations of Ni and Al in the decomposition zone was noted that would correlate with the formation of γ'-phase as a product of MC decomposition.

The EDS spectrum of the core of the degenerated primary MC carbide (Fig. 7) is similar to that of the original MC carbides in the shank, its composition being (Ti, Ta)C. The

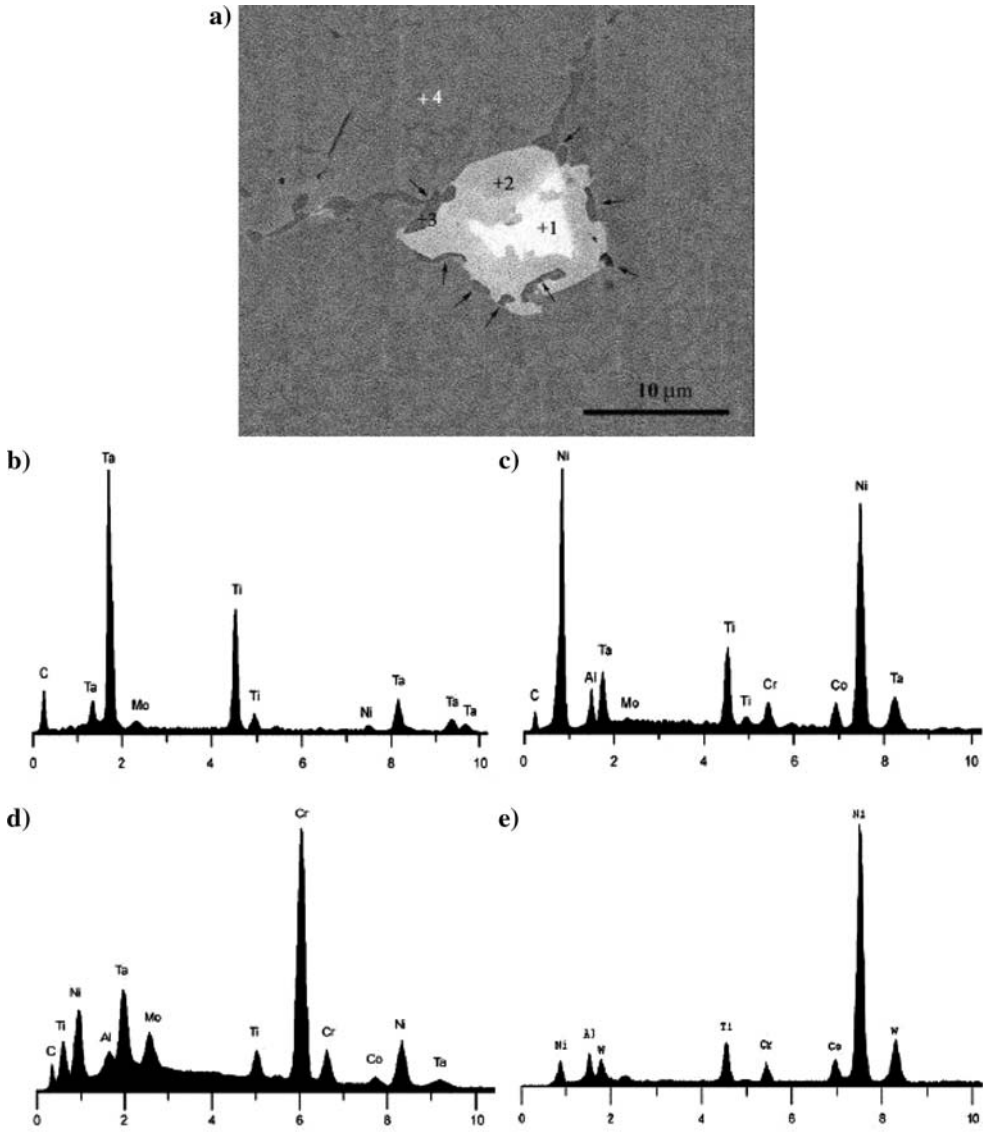

Fig. 7 SEM-BEI micrograph (a) and EDS spectra (b-e) of Blade 1 leading edge specimen. Arrows in (a) indicate discrete $M_{23}C_6$ carbides formed at the periphery of MC decomposition zone. The EDS spectra from marked (+) locations in (a) are shown: 1—original MC core (b); 2—MC decomposition zone (c); 3—$M_{23}C_6$ carbide (d); 4—γ'-phase (e)

discrete particles formed at the edges of the original MC carbides were identified as Cr-rich $M_{23}C_6$ carbides.

Contrary to the currently accepted reaction, the γ'-phase formation as a product of MC decomposition was not confirmed. The EDS spectra from the decomposition zone surrounding the original MC core showed the presence of a considerable amount of carbon, so that the phase from which they were taken cannot be γ'(The comparison of the spectrum from the primary γ' in Fig. 7(e) with that obtained from the decomposition zone (Fig. 7c) illustrated the difference. The spectrum of the decomposition zone was similar to that of the MC carbide (Fig. 7b), with parts of Ti and Ta replaced with Ni, Co, and Cr.

The TEM study also confirmed the absence of γ'-phase in the MC decomposition zone (Fig. 8). A phase other than γ', containing high amounts of Ni, as was established by EDS, was observed at the periphery of the MC decomposition zone in both blades (Fig. 8a). A TEM analysis revealed the presence of the hexagonal close-packed Ni_3Ti η-phase. Convergent beam electron diffraction and standard selected area electron diffraction methods were used to identify the crystal structure of this phase as $P6_3/mmc$ with lattice parameters $a \sim 0.52$ nm, $c \sim 0.82$ nm (Fig. 8b, c). The EDS analysis characterized the chemical composition of η-phase observed in both blades as $Ni_3(Ti, Ta)$ (Fig. 8d). The orientation relationship exists between this phase and the γ matrix:

$$\{111\}_\gamma || (0001)_\eta, \quad \langle 110\rangle_\gamma || \langle 11\bar{2}0\rangle_\eta. \tag{Eq 2}$$

The presence of $M_{23}C_6$ carbides and η-phase next to the primary MC carbide was found in the airfoil specimens from both blades. In the light of these observations, the MC decomposition reaction can be presented as

$$MC + \gamma \rightarrow M_{23}C_6 + \eta. \tag{Eq 3}$$

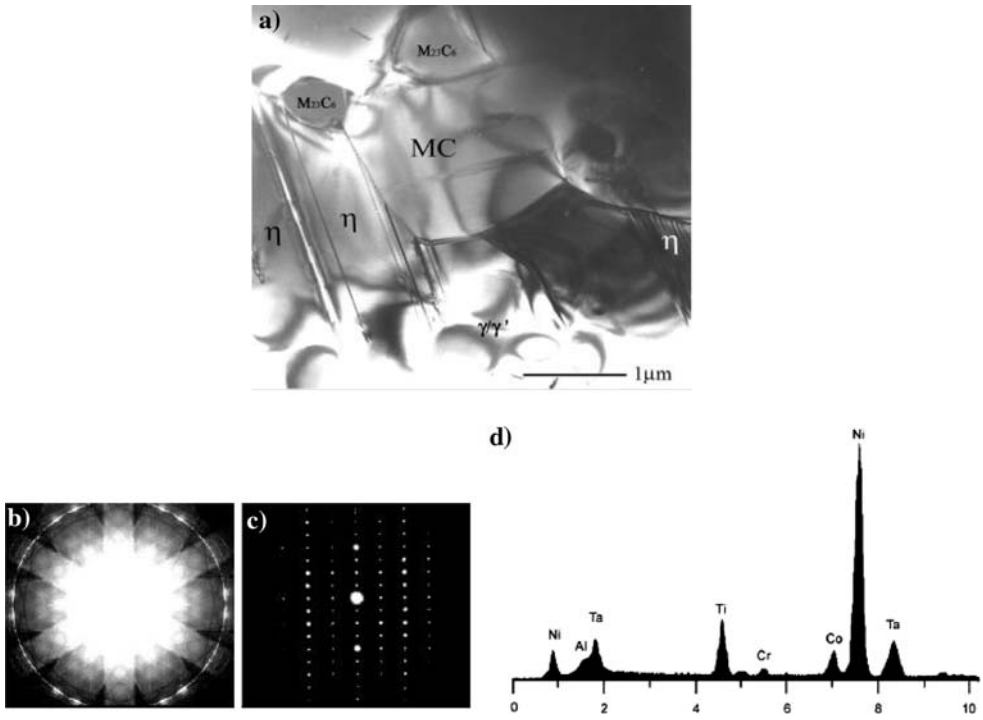

Fig. 8 Bright-field TEM micrograph of the MC decomposition zone in Blade 1 leading edge specimen (a). [0001] convergent-beam diffraction pattern (b), [11$\bar{2}$0] SADP (c) and EDS spectrum (d) of η-phase

Table 2 Stress-rupture test results for Blade 1

	Shank specimens				Airfoil specimens				
Stress-rupture test results	**1**	**2**	**3**	**Average**	**1**	**2**	**3**	**4**	**Average**
Time to fracture, h	128.9	118.4	122.4	123.2	32.9	30.5	29.2	34.1	31.7
Elongation, %	9.3	8.3	8.9	8.8	5.2	5.1	4.8	5.2	5.1
Reduction in area, %	12.3	11.2	11.7	11.7	7.2	7.1	6.9	7.5	7.2

Table 3 Stress-rupture test results for Blade 2

	Shank specimens				Airfoil specimens				
Stress-rupture test results	**1**	**2**	**3**	**Average**	**1**	**2**	**3**	**4**	**Average**
Time to fracture (t), h	156.2	133.8	146.8	145.6	13.7	15.8	16.9	14.1	15.1
Elongation, %	12.8	10.7	11.6	11.7	4.9	5.0	5.1	4.9	4.9
Reduction in area, %	21.9	18.6	19.2	19.9	6.8	7.1	7.2	6.9	7.0

A more detailed description of the η-phase formation during the MC carbide decomposition can be found in our earlier work (Ref 13).

3.3 Stress-Rupture and Microhardness Testing

The service-induced microstructural changes in the airfoils caused a significant degradation of the material properties. The results of the stress-rupture tests of Blade 1 and Blade 2 presented in Table 2 and 3, respectively, and in Fig. 9 demonstrated a dramatic reduction of the airfoil stress-rupture life compared with those of the shank in both blades. The ductility of the airfoil specimens decreased noticeably as well.

The microhardness of the γ/γ′ matrix was measured in order to evaluate the degree of the solution-strengthening and the precipitation-hardening effects, which correlates with the degree of the alloy overaging. The results presented in Table 4 and Fig. 10 demonstrated a significant decrease in the airfoil microhardness compared to that of the shank in both blades.

In order to make a comparison of the test data easier and to minimize the deficiency of relatively short-term tests, the stress-rupture life reduction rates for both blades were calculated as the difference between the shank time to fracture (t^{Sh}) and airfoil time to fracture (t^{Af}) relative to the shank time to fracture, $(t^{Sh} - t^{Af})*100/t^{Sh}$ (Fig. 11).

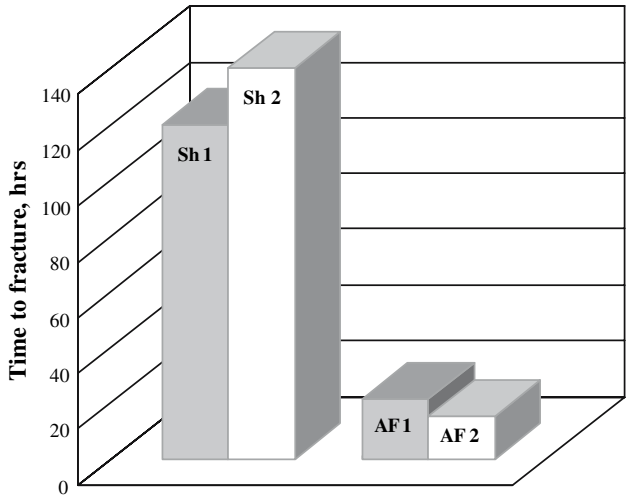

Fig. 9 Stress-rupture test results. Sh1 and Sh2—shank specimens of Blade 1 and Blade 2, respectively. AF 1 and AF 2—airfoil specimens of Blade 1 and Blade 2, respectively

Table 4 Microhardness (H_v) test results

Blade 1			Blade 2		
Shank	Leading edge	Trailing edge	Shank	Leading edge	Trailing edge
433	362	359	446	347	343

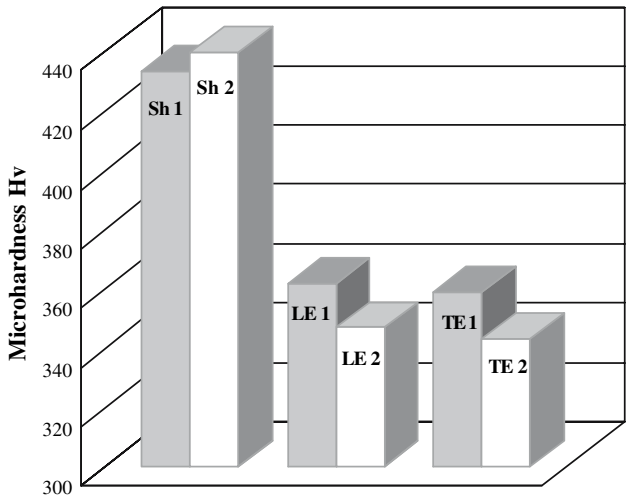

Fig. 10 Microhardness test results. Sh1 and Sh2—shank specimens of Blade 1 and Blade 2, respectively. LE1 and LE2—leading edge specimens of Blade 1 and Blade 2, respectively. TE1 and TE2—trailing edge specimens of Blade 1 and Blade 2, respectively

Similarly, the aging rates were calculated as the difference between microhardness values of the shank and the airfoil (as an average of the microhardness values of the leading edge and trailing edge) relative to the shank microhardness, $(H_v^{Sh} - H_v^{Af})*100/H_v^{Sh}$ (Fig. 12).

Comparing the data presented in Fig. 11 and 12, it can be noted that the decrease in the airfoil time to fracture and

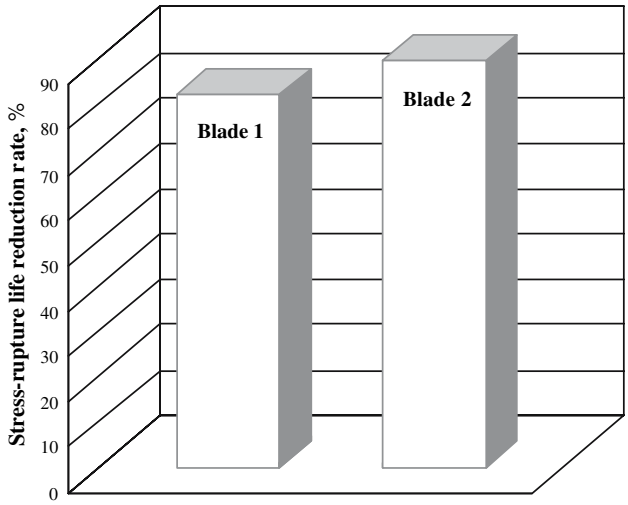

Fig. 11 Stress-rupture life reduction rate calculated as the difference between the shank time to fracture (t^{Sh}) and airfoil time to fracture (t^{Af}) relative to the shank time to fracture, $(t^{Sh} - t^{Af})*100/t^{Sh}$

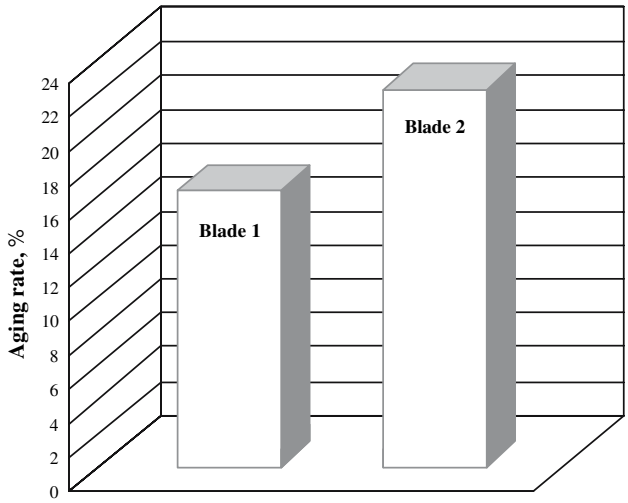

Fig. 12 Aging rate calculated as the difference between the shank and airfoil microhardness relative to the shank microhardness, $(H_V^{Sh} - H_V^{Af})*100/H_V^{Sh}$

microhardness of the rejuvenated Blade 2 was considerably more advanced than that of the new Blade 1. This fact indicates that, although the processes taking place in both blades during service were similar, as has been shown earlier, there were evidently certain differences present in the resulting microstructures.

These differences are quite obvious. It can be seen that secondary $M_{23}C_6$ carbide precipitation at the grain boundaries in Blade 2 is noticeably more prominent compared to that in Blade 1 (Fig. 13a, b). The growth of primary γ' particles in Blade 2 is much more advanced than in Blade 1 (Fig. 13c, d): the average primary γ' particle diameter in Blade 1 is 1.28 μm, average γ' diameter in Blade 2 is 1.87 μm. Practically all fine secondary γ' particles were consumed by the grown primary γ' in Blade 2 (Fig. 13d).

Since the shank microstructures of both blades were identical and typical for a new alloy, it was safe to presume that rejuvenating heat treatment of Blade 2 did not contribute to the changes of the microstructure of its airfoil.

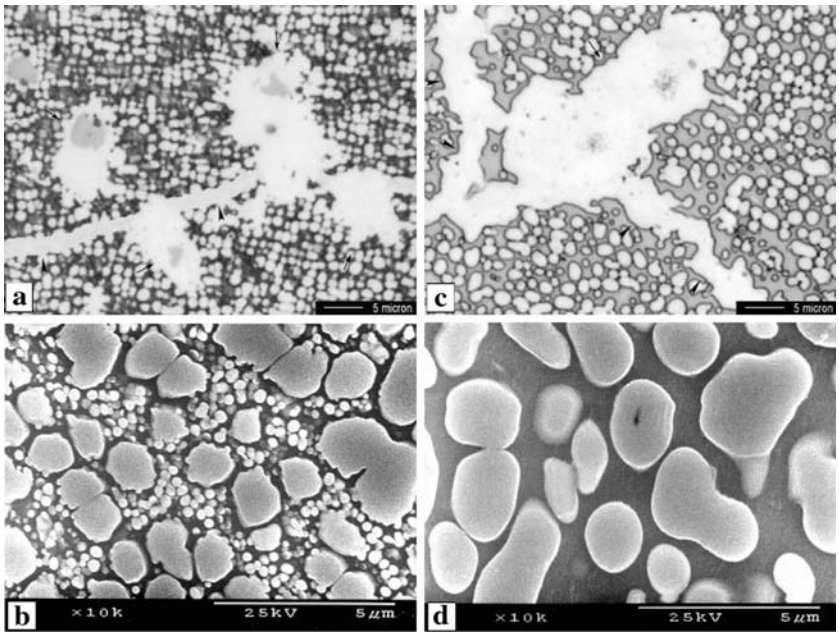

Fig. 13 Optical (a, c) and SEM (b, d) micrographs of the Blade 1 and Blade 2 leading edge specimens. a, b—Blade 1; c, d—Blade 2 (Etchant—electrolytic chromic acid). Arrows indicate degenerated primary MC carbides; arrowheads indicate excessive secondary M23C6 carbides at the grain boundaries

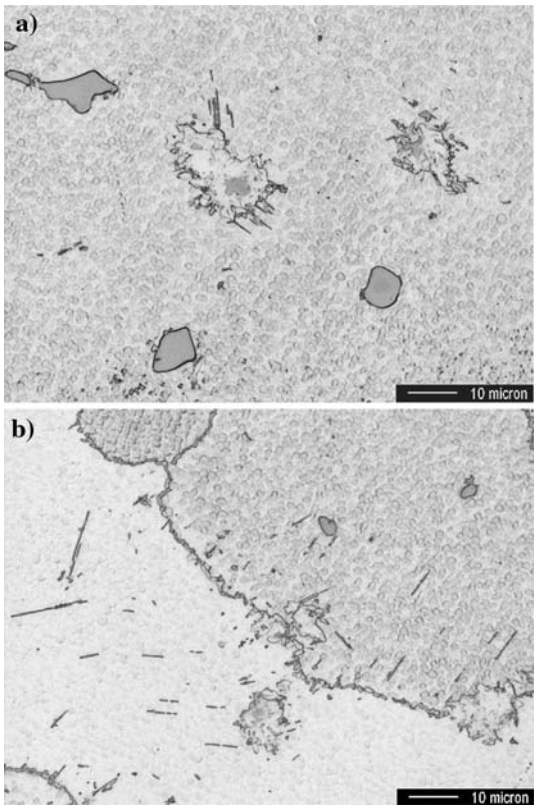

Fig. 14 Optical micrographs of the leading edge specimens of Blade 1 (a) and Blade 2 (b) (Etchant—Kalling's reagent)

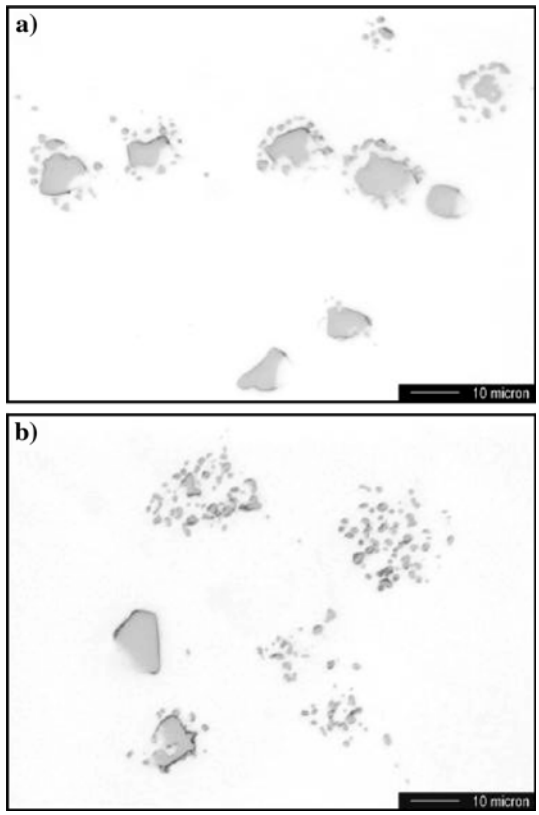

Fig. 15 Optical micrographs of the degenerated primary MC carbides in the leading edge specimens of Blade 1 (a) and Blade 2 (b) (As-polished)

It should be noted also that there was a considerably larger amount of the lath-like $M_{23}C_6$ carbides formed on the stacking faults in the grain interiors in Blade 2 than in Blade 1 (Fig. 14). All these facts indicated an accelerated aging of the rejuvenated Blade 2 microstructure in comparison with that of the new Blade 1. In addition, degenerated MC carbides in Blade 2 appeared much more fragmented compared with Blade 1 (Fig. 15).

Table 5 Volume fractions of decomposed MC carbides in the Blade 1 and Blade 2 leading edge specimens

Blade 1				Blade 2			
	Volume fraction				Volume fraction		
Field	Matrix	MC dec.	MC	Field	Matrix	MC dec.	MC
1	98.74	0.75	0.49	1	97.57	1.73	0.39
2	97.81	1.81	0.36	2	96.86	1.95	0.80
3	98.42	0.82	0.69	3	97.41	1.63	0.69
4	98.87	0.37	0.49	4	97.08	1.82	0.82
5	98.47	1.02	0.47	5	97.65	1.37	0.65
6	98.09	1.39	0.49	6	97.33	1.65	0.67
7	99.05	0.55	0.41	7	97.27	1.51	0.84
8	99.34	0.2	0.45	8	97.19	1.26	1.27
9	99.22	0.55	0.23	9	97.23	1.60	0.84
10	98.77	0.75	0.48	10	97.72	1.36	0.64
Averages	98.678	0.821	0.456	Averages	97.799	1.588	0.613
SD	0.48632	0.4816	0.116161	SD	0.265642	0.217041	0.22472
f_{MCdec}/f_{MC} = 1.80				f_{MCdec}/f_{MC} = 2.59			

The volume fraction of the decomposed MC carbides (f_{MCdec}) versus the volume fraction of original MC carbides (f_{MC}) was determined using the quantitative backscattered electrons image analysis (Table 5). It was shown that the relative volume fraction of the decomposed MC carbides in Blade 2 (f_{MCdec}/f_{MC} = 2.59) was bigger than in Blade 1 (f_{MCdec}/f_{MC} = 1.80).

The presented data demonstrated an obvious acceleration of aging processes in the rejuvenated blade. Such a difference in the behavior of a new blade and a rejuvenated one appears to be related to the primary MC carbide decomposition. It is well known that a solution-and-age rejuvenating heat treatment is able to restore an overaged microstructure of the Ni-base superalloy and its properties by eliminating excessive grain-boundary $M_{23}C_6$ carbides and re-precipitating γ'-phase in a favorable bimodal morphology. While coarsening and coalescence of γ'-phase and excessive grain-boundary $M_{23}C_6$ carbide precipitation are reversible, primary MC carbide decomposition cannot be reversed. The presence of the decomposed MC carbides is what differs the microstructure of rejuvenated blade from that of a new one.

As has been shown earlier (Ref 13), the MC decomposition involves the diffusion of carbon from the MC carbide in the outward direction and the diffusion of Ni, Cr, and Co from the γ-matrix into the MC in the opposite direction creating the environment favorable for the formation of the lower-order $M_{23}C_6$ carbides and η-phase on the MC/γ-matrix interface.

It has been found that the degenerated MC carbide demonstrate a gradual change of the elemental distribution from its center towards the periphery: the farther from the MC carbide center, the less carbon and more Ni, Cr, and Co it contains (Ref 13). The replacement of the strong carbide-forming atoms, such as Ti and Ta, with Ni, Co, and Cr atoms, is known to weaken the interatomic bonds in the MC carbide resulting in a decrease of its stability. Although the original MC carbides are very stable (up to the melting temperature), the degenerated lower-carbon MC can become unstable at much lower temperature.

At the solution stage of rejuvenating heat treatment, the products of the MC carbide decomposition (a lower-carbon degenerated part of the MC carbides, η-phase, and $M_{23}C_6$ carbides) are dissolved into the γ-matrix leaving behind fragments of the original primary MC carbides, as shown in Fig. 14. Dissolving of the degenerated parts of the primary MC carbides, η-phase, and the abundant $M_{23}C_6$ carbides formed as a result of the MC decomposition causes a release of additional amounts of carbon and carbide-forming elements, such as Ti and Ta, that were originally tied up in the primary MC carbides, into the γ-matrix. The resulting change in the elemental composition of the matrix appears to be the cause of the accelerated aging in the rejuvenated blade in the next service cycle.

A change in the elemental composition of the matrix can cause a larger γ/γ' lattice mismatch leading to a considerable loss of γ'-phase coherency and, consequently, to the accelerated growth of cuboidal γ' particles (Ref 14). The increased concentration of carbon in the matrix resulted in a heavier secondary $M_{23}C_6$ carbide precipitation at the grain boundaries and in the grain interiors, subsequently weakening the grain boundaries and the matrix. A combination of these processes apparently caused the accelerated degradation of the rejuvenated blade microstructure and properties.

Rejuvenation of the industrial gas turbine blades proved to be able to extend the part life and was used successfully. However, users often delay repairs causing an advanced degradation of the material. In this case, rejuvenation may not provide the expected life extension for reasons discussed in this study. In order to prolong the blade's life it would be advisable to avoid the extensive primary MC carbide decomposition by reducing the periods between rejuvenations, thus preventing an advanced development of this process. More frequent rejuvenations will extend the blade life and, despite the extra cost of additional rejuvenations, will save money on the blade replacement in the long run.

4. Conclusions

1. Two conventionally cast GTD-111 industrial gas turbine blades, one new and the other refurbished, removed from the same machine after a particular operational cycle, were studied. The objective of this investigation was to determine the effect of rejuvenation on the material behavior during service.

2. Service-induced microstructural changes in the airfoil of both blades consisted of γ'-phase coarsening and coalescence, excessive secondary $M_{23}C_6$ carbides precipitation at the grain boundaries, and primary MC carbides decomposition. The microstructure degradation caused a significant deterioration of the alloy properties.
3. Both blades displayed similar primary MC carbide decomposition mechanism. The degenerated MC carbides exhibited the presence of a diminished core of the original carbide surrounded by a well-defined decomposition zone, with $M_{23}C_6$ carbides formed at its periphery.
4. Hexagonal Ni_3(Ti, Ta) η-phase was discovered in the MC decomposition zone and on the MC-γ/γ' interface in both blades. The proposed reaction of primary MC carbide decomposition can be described as $MC + \gamma/\gamma' \rightarrow M_{23}C_6 + \eta$.
5. It was found that service-induced changes in the microstructure, such as γ'-phase coarsening and agglomeration, excessive secondary $M_{23}C_6$ carbide precipitation at the grain boundaries, and primary MC carbides decomposition, were considerably more advanced in the rejuvenated blade. The stress-rupture life and microhardness of the rejuvenated blade were decreased significantly compared to those of the new blade after the same number of hours in service.
6. Primary MC carbide decomposition was shown to have a significant effect on the aging kinetics of rejuvenated material, which was evidently related to a release of additional amounts of carbon and carbide-forming elements into the matrix during rejuvenating solution heat treatment. This process caused the acceleration of the aging of rejuvenated blade in the next service cycle. The detrimental effect of the MC decomposition can be minimized by reducing the periods between rejuvenations.

Acknowledgments

The author would like to thank Dr. Vladi Levit, senior research scientist, the Department of Material Science and Engineering, The Ohio State University, and Dr. Michael J. Kaufman, professor and chair of the Department of Material Science and Engineering, University of North Texas, for a valuable discussion. The author also acknowledges the use of the analytical facilities in the Major Analytical Instrumentation Center of University of Florida during the course of this work.

References

1. R.A. Stevens and P.E.J. Flewitt, Microstructural Changes which Occur During Isohronal Heat Treatment of the Nickel-Base Superalloy IN-738, *J. Mater. Sci.*, 1978, **13**, p 367–376
2. R.A. Stevens and P.E.J. Flewitt, The Effect of γ'-Precipitate Coarsening During Isothermal Aging and Creep of the Nickel-Base Superalloy IN-738, *Mater. Sci. Eng.*, 1979, **37**, p 237–247
3. C.T. Sims, N.S. Stoloff, and W.C. Hagel, Eds., *Superalloys II*, John Wiley & Sons, New York, NY, 1984, p 97–113
4. A.K. Koul and R. Castillo, Assessment of Service-Induced Microstructural Damage and Its Rejuvenation in Turbine Blades, *Metall. Trans. A*, 1988, **19A**, p 2049–2066
5. M. Durrand-Charre, *The Microstructure of Superalloys*. Gordon and Breach Science Publishers, Amsterdam, The Netherlands, 1997
6. J.A. Daleo and J.R. Wilson, GTD111 Alloy Material Study, *J. Eng. Gas Turbines Power*, 1998, **120**, ASME paper no. 96-GT-520
7. R.A. Stevens, and P.E.J. Flewitt, Regenerative Heat Treatments for the Extension of the Creep Life of the Superalloy IN-738. Strength of the Metals and Alloys, *5th Int. Conf.*, Aug. 27–31, 1979 (Aahen, Germany), Pergamon Press, Elmsford, NY, 1979, vol. 1, p 439–444
8. J.C. Beddoes and W. Walace, Heat Treatment of Hot Isostatically Processed IN-738 Investment Castings, *Metallography*, 1980, **13**, p 185–194
9. A. Baldan, Extension of the Creep Life of a Conventionally Cast Nickel-Base Superalloy by Regenerative Heat Treatment, *Proc. Conf. "Materials Aging and Component Life Extension*, Oct. 10–13, 1995 (Milan, Italy), Engineering Materials Advisory Services Ltd., United Kingdom, 1995, vol. II, p 943–950
10. J. Hakl, V. Bina, J. Kudrman, and R. Pech, Blade Life Prolongation in Land Based Gas Turbines, *Proc. Conf. "Materials Aging and Component Life Extension*, Oct. 10–13, 1995 (Milan, Italy), Engineering Materials Advisory Services Ltd., United Kingdom, 1995, vol. II, p 991–1000
11. E. Lvova and D. Norsworthy, Influence of Service-Induced Microstructural Changes on the Aging Kinetics of Rejuvenated Ni-Based Superalloy Gas Turbine Blades, *J. Mater. Eng. Perform.*, 2001, **10**(3), p 299–313
12. H. Xuebing, K. Yan, Z. Huihua, Z. Yun, and H. Zhuangqi, Influence of the Heat Treatment on the Microstructure of a Unidirectional Ni-Base Superalloy, *Mater. Lett.*, 1998, **36**, p 210–213
13. G. Lvov, V.I. Levit, and M.J. Kaufman, Mechanism of Primary MC Carbide Decomposition in Ni-Base Superalloys, *Metall. Trans. A*, 2004, **35A**, p 1669–1679
14. H.M. Tawancy, N.M. Abbas, A.I. Al-Mana, and T.N. Rhys-Jones, Thermal Stability of the Advanced Ni-Base Superalloys, *J. Mater. Sci.*, 1994, **29**, p 2445–2458